Appl. Phys. B 56, 209–221 (1993)

Applied Physics B Photophysics and Laser Chemistry

Self-Consistent Modelling of X-Ray Preionized XeCl-Laser Discharges

E. Estocq[1,2], **G. Delouya**[1], **J. Bretagne**[1]

[1] Laboratoire de Physique des Gaz et Plasmas, U.A. au C.N.R.S., Université Paris-Sud, Bât. 212, F-91405 Orsay Cédex, France
[2] SOPRA, 26 rue P. Joigneaux, F-92270 Bois-Colombes, France

Received 15 October 1992/Accepted 28 December 1992

Abstract. In this theoretical work a 0-D model for a self-sustained X-ray preionized XeCl-laser discharge is presented. The model is self-consistent in the sense that it simultaneously solves, contrarily to the usual decoupling procedure, the Boltzmann equation for electrons, the kinetic equations for excited and ionic species, the equations for the electrical circuit and the laser photon density. It includes a rather complete kinetics of HCl(v) vibrational excitation, dissociation and dissociative attachment. The influence of electron collisions with excited species and of e–e Coulomb collisions on the plasma parameters and transport coefficients is discussed. Some evidence of the non-stationary equilibrium between the electron distribution and the reduced electric field E/N is given. Results of the model are compared with experimental ones corresponding to a XeCl-laser discharge driven by a L–C inversion circuit. The model predicts well the main trends for the variation of the laser energy in a large range of experimental conditions. The discrepancy between experiment and model for absolute values of the laser energy is discussed.

PACS: 42.55.G, 52.25, 82.20

A large amount of theoretical works has already been devoted to the modelling of xenon chloride lasers either excited by e-beams [1–4] or by preionized electrical discharges [5–10]. Some early works on the modelling of excimer lasers were done within the assumption of a Maxwellian electron energy distribution function (eedf) [1]. It is now clear that this assumption is not realistic, it overestimates the influence of excited and ionized species of the lightest rare gas. So, it implies that, in some manner, the non-Maxwellian eedf calculation has to be included in the model.

We generally want to couple the microscopic behaviour of the discharge to the macroscopic parameters of the electrical circuit, including the laser cavity itself, and we need to know the transport parameters of the plasma (electron drift velocity and mobility or equivalent plasma resistance). These parameters must also be deduced from the knowledge of the eedf.

Furthermore, the situation is not well established about the different species and channel reactions which are to be included in a laser model. For instance, to what detail the excited states of rare gas atoms must be described? Hammer and Bötticher [11], in connection with absorption spectroscopy measurements, considered two xenon excited states and discussed the role of these states and the effect of transitions between them. In recent papers, Kannari et al. [4] and Johnson et al. [3] proposed to take account of three effective excited levels for the xenon atom.

In the very recent literature, one of the major points on which attention was focused is the influence of the HCl(X, v) vibrational distribution. It is well known that, in attaching gases, the process of dissociative attachment is strongly dependent on the vibrational excitation of the molecule. Until recently, this problem had not received great attention and the number of vibrational levels HCl(X, v) which were included in the models were limited: two levels by Levin et al. [1] and Hokazono et al. [6], three by Gorse [12], and four by Demyanov et al. [10], and by Hammer and Bötticher [11] . A recent paper by Gorse et al. [13] considered in itself, for conditions typical of discharge-pumped XeCl lasers, the complete kinetics of the vibrational distribution of HCl(X, v) including competing direct dissociation of HCl by electron impact, V–V exchanges, V–T deactivating processes. This paper concluded on the need to include a larger number of vibrational HCl(v) levels in XeCl laser models and to consider processes which are usually neglected. Preliminary results for such a model were given by Capitelli et al. [14]. Another point about HCl influence was discussed by Lando et al. [15]; they studied the temporal evolution of the electron density in an electron-beam excited Ar/HCl discharge, in order to improve the agreement between results for experiment and modelling, suggested to include the effect of non-equilibrium rotational distribution of HCl.

Furthermore, some other processes such as electron–electron Coulomb collisions which greatly increase the CPU time, are often not considered in the calculation of the eedf.

The model that we develop in this paper is first characterized by its self-consistency: rather than solving the Boltzmann equation separately on different time scales for the eedf, the kinetic equations for excited and ionized species and the electrical equations for the circuit, we simultaneously solve these three sets of time-differential equations. This point can be important due to the fact that during its history the discharge presents fast variations of parameters, for instance of the reduced electric field E/N, and the usual assumption of a quasi-stationary equilibrium of the eedf with E/N can be questionable. This point was already discussed in detail in a recent paper of Winkler and Wuttke [16]. These authors showed that the validity of this assumption depends mainly of the respective values of frequencies associated to the electric field evolution and inelastic collisions.

Second, on the basis of the previous work of Gorse et al. [13] and in parallel with a recently published work of Longo et al. [17], we developed a rather complete kinetics of HCl(X, v). As in this last work, we have included seven vibrational levels of HCl(X) to be sure to obtain, at each time of the discharge, the convergence of the effective dissociative attachment towards its limit and a good representation of the HCl kinetics.

We first describe the numerical code including some details about the self-consistent treatment. This code is used for a typical electrical circuit used by SOPRA [18]. The results that we present are sufficiently general to be of interest for other conditions. Finally, we compare the results of the model with available experimental data and we discuss these results.

1 Description of the Model

Any model for a pulsed laser discharge must include the coupling between the electrical circuit which provides the energy, the plasma electrons to which a part of the energy stored in the electrical circuit is transferred and the excited and ionic species which are created by electron collisions. In addition, we must take into account the initial conditions of the system yielded by the actual preionization. The main assumption of the model that we present here, is that the active medium is assumed to be homogeneous. We first describe the main levels which are accounted for, the main reactions that we include. As a guidance for the effective levels that we consider, we have tried to connect these levels with the possibility of detecting, either by emission or absorption spectroscopy, transitions between these effective levels. This model can be used for any experimental device. We present its description and results for the SOPRA laser [18–20]. The active medium is excited by an X-ray preionized transverse-electric discharge driven by a LC-inversion circuit. The laser mixture is typically of about 99% of neon, 1% of xenon and 0.1% of HCl.

1.1 Species, Levels and Processes Included in the Model

In order to study the influence of excited states for various gas compositions, including Ne/HCl and Ne/Xe mixtures, we have included in our model a rather detailed description of neon and xenon excited states. The schematic diagram for the effective levels of the two rare gases is represented in Fig. 1. The kinetic equations include the temporal evolution of 38 species.

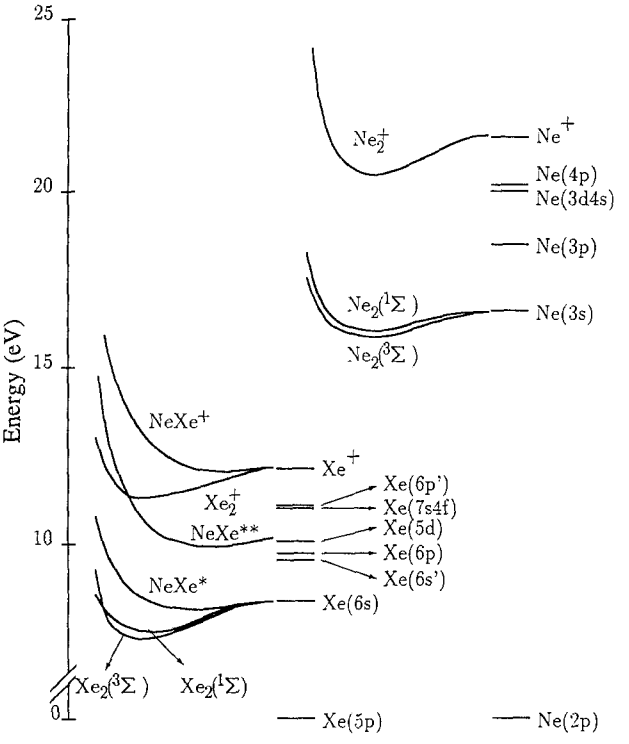

Fig. 1. Neon and xenon levels included in kinetic reactions

For neon we have considered the ground state Ne($2p$), four atomic excited levels [Ne($3s$), Ne($3p$), Ne($3d$, $4s$), and Ne($4p$)], two molecular levels [$Ne_2(^3\Sigma)$ and $Ne_2(^1\Sigma)$], and Ne^+ and Ne_2^+ ions.

For xenon we have included the Xe($5p$) ground state, six excited atomic levels [Xe($6s$), Xe($6s'$), Xe($6p$), Xe($6p'$), Xe($5d$), and an effective level which groups the $7s$, $7p$, $6d$, and $4f$ configurations], two molecular levels [$Xe_2(^3\Sigma)$ and $Xe_2(^1\Sigma)$], the Xe^+ atomic ion, and the Xe_2^+ molecular ion.

We have taken account of the three heteronuclear molecules NeXe*, NeXe**, $NeXe^+$. We will discuss the influence of the $NeXe^+$ ion. As previously mentioned, we have considered for HCl seven vibrational levels HCl(X, v), $v = 0$ to $v = 6$, and the species involving dissociated products of the HCl molecule.

Finally, as exciplex molecules we have considered one dimer molecule XeCl*, which corresponds to the molecular state XeCl($B^2\Sigma$), the slightly bound state XeCl(X), and the trimer molecule Xe_2Cl^*.

Returning to the problem of HCl(X, v) vibrational distribution, we have included the same processes and used the same formalism as in the paper of Gorse et al. [13] for the vibrational master equations. This means, that in addition to vibrational exchange by electron collision (inelastic and superelastic e–V processes) and dissociative attachment leading to Cl^- formation, which are included in all the models, we consider additional processes such as redistribution of vibrational quanta by vibration-vibration exchanges (V–V processes), deactivation of vibrational

excited states by vibration–translation exchanges (V–T processes), direct dissociation of HCl by electron impact, associative detachment, three-body recombination of H and Cl and radiative de-excitation of HCl(v).

The data which are needed for the modelling of the HCl kinetics were in general taken from the Bari group [21]. Cross-sections for dissociative attachment were taken from Teillet-Billy and Gauyacq [22]. We included in these data the effect of the rotational distribution corresponding to the room gas temperature $T_g = 300$ K [23].

The physical processes accounted in the model include elastic, inelastic, superelastic and ionization electron collisions, Penning ionization, dissociative recombination, dissociative attachment on HCl(v), absorption of laser photons by kinetic species leading either to photodissociation or photoionization, and classical two and three-body collision between kinetic species. All the kinetic processes involving electrons are included in the Boltzmann equation.

Data corresponding to two-and three-body collision rates between heavy particles were mainly taken from the recent paper of Kannari et al. [4]. About 450 kinetic reactions were included in the model. Among them a non-negligible part is connected with the HCl(v) kinetics. All these kinetics reactions are ordered by process category, i.e., for instance, inelastic and superelastic electron collisions, ionization, radiative transitions, etc. They are introduced through an input data file in which we define the species which are considered, give the kinetic reactions and code them. A compilation of these data is given in [20], as well as the description of the semi-automatic manner in which they are accounted for in the numerical code.

The evolution equation of laser photon density in the optical cavity was treated as in [5]. This equation was considered as a kinetic equation.

1.2 Boltzmann Equation

The electron energy distribution function (eedf) is determined from the time dependent Boltzmann equation within the two-term expansion approximation and which is numerically solved through the formalism used in previous papers [25, 26]. This equation is written as

$$\frac{\partial n(\varepsilon,t)}{\partial t} = \frac{\partial J_F(\varepsilon)}{\partial \varepsilon} + \frac{\partial J_{el}(\varepsilon)|_{e-n}}{\partial \varepsilon} + \frac{\partial J_{el}(\varepsilon)|_{e-e}}{\partial \varepsilon} + K_{ion} + K_{inel} + K_{sup} + K_{da} + K_{rec} + S(\varepsilon,t)\,, \tag{1}$$

where $n(\varepsilon,t)$ represents the electron number density in the energy range $[\varepsilon, \varepsilon + d\varepsilon]$ at time t. The right-hand side expression includes the electric field heating and all collisional processes in whic.h the plasma electrons are involved. The J terms correspond to fluxes of electrons in the energy space driven respectively by the applied electric field $[J_F(\varepsilon)]$ the elastic electron-heavy species $(J_{el}(\varepsilon)|_{e-n})$ and the e–e Coulomb collisions $(J_{el}(\varepsilon)|_{e-e})$. K_{ion} corresponds to ionization by electron collision as well as Penning ionization or photoionization, K_{inel} to inelastic collisions, K_{sup} to superelastic collisions, K_{da} to dissociative attachment, K_{rec} molecular ion dissociative recombination, and $S(\varepsilon,t)$ is a source term due to the X-ray preionization. Explicit expressions for the various terms of the right-hand side of (l) can be found in previous papers [24–26].

We must mention some particular points relevant to processes included in the Boltzmann equation:

– For electron collisions involving the Ne and Xe ground states we used the cross-section data proposed by Puech and Mizzi [27]. The set of corresponding semi-empirical cross-sections was tested against transport coefficients obtained from swarm experiments.

– For inelastic and superelastic transitions between effective excited states by electron impact, we only considered those which correspond to optically allowed transitions. The corresponding cross-sections have been taken to be given by

$$\sigma_{ij}(\varepsilon) = 4\pi a_o^2 (\mathrm{Ry}/E_{ij})^2 f_{ij}(1 - 1/U_{ij}) \ln(1.25\, U_{ij})/U_{ij}\,, \tag{2}$$

in which ε is the energy of incident electrons, a_o the Bohr radius, Ry the Rydberg constant, E_{ij} the energy difference between levels i and j, f_{ij} the oscillator strength for the i–j transition, and U_{ij} the reduced energy $U_{ij} = E/E_{ij}$. f_{ij} values have been deduced from transition probabilities mainly taken from Wiese et al. [28] for neon and from Aymar and Coulombe [29] for xenon. Average values obtained for transitions between effective excited states are reported in [20].

– All ionization processes are considered with non-zero energy for emitted electrons. This means that we need approximations for the energy differential cross-sections which were taken from Puech and Mizzi [27] for ionization of Ne and Xe ground states and from Bretagne et al. [25] for ionization of excited states.

– For Penning processes and photoionization, issuing electrons are introduced as source terms at finite energies according to energy conservation in the collision.

1.3 Coupling Between Electric Circuit and Plasma

The coupling of the plasma with the electrical circuit was introduced through the power density P injected in the discharge and was calculated at each time step.

From a microscopic aspect, P was obtained from the Boltzmann equation as being:

$$P = \int_0^\infty J_F(\varepsilon) d\varepsilon\,, \tag{3}$$

where $J_F(\varepsilon)$ is the electron energy flux in the energy space driven by the electric field heating. It is written as

$$J_F(\varepsilon) = \frac{2}{3}\frac{e^2}{m_e} N \left(\frac{E}{N}\right)^2 \frac{\varepsilon}{\nu_{en}(\varepsilon)} \left(\frac{\partial n(\varepsilon,t)}{\partial \varepsilon} - \frac{n(\varepsilon,t)}{2\varepsilon}\right). \tag{4}$$

In this equation, $\nu_{en}(\varepsilon) = \sum_j (N_j/N) v \sigma_{en,j}(\varepsilon)$ is the frequency for total cross-sections in electron–atom and electron–molecule collisions summed over the contributions of the j species with densities N_j, N the total density of atoms and molecules and E/N the reduced electric field. Instead of the integral of the right-hand side of (3), we introduced the reduced flux J_E which was expressed as:

$$J_E = \left(\frac{E}{N}\right)^{-2} \int_0^\infty J_F(\varepsilon)d\varepsilon$$

$$= \frac{2}{3}\frac{e^2}{m_e}N \int_0^\infty \frac{\varepsilon}{\nu_{en}(\varepsilon)}\left(\frac{\partial n(\varepsilon,t)}{\partial\varepsilon} - \frac{n(\varepsilon,t)}{2\varepsilon}\right)d\varepsilon . \quad (5)$$

J_E/N depends only on the eedf $n(\varepsilon, t)$ and its first derivative $\partial n(\varepsilon, t)/\partial\varepsilon$.

From a macroscopic aspect (Ohm's law), we wrote:

$$P = I_d E/A , \quad (6)$$

where I_d is the discharge current and A the discharge area. The current density I_{sd}/A was obtained from (3, 5, 6) and written as

$$I_d/A = (E/N)(J_E/N) . \quad (7)$$

J_E/N is the reduced energy flux driven along the energy axis corresponding to one atom or molecule. As explicited later, this term was numerically expressed in terms of the eedf $n(\varepsilon, t)$ from integral (5) written in discrete form. If we consider I_d as an independent variable, then E/N is a secondary variable which is obtained at each time from (7).

The drift velocity (W_d) is obtained from relation (7) and from its expression in terms of the discharge current density I_{sd} and the electron number density n_e and is written:

$$I_{sd} = en_e W_d .$$

Then

$$W_d = \frac{1}{en_e}\frac{EJ_E}{N^2} .$$

W_d is an important parameter for testing the influence of various parameters, cross-section data and assumptions used in the model.

1.4 Electric Circuit

The scheme of the electric circuit of the SOPRA laser [18] is shown in Fig. 2. Electric energy is stored in two capacitor banks C_1 and C_2. First, the capacitors are charged to a given charging voltage V_C (up to 50 kV), C_2 is charged through the inductance coil L_3 to $-V_C$. When, the thyratron is switched on, the voltage of C_1 capacitor bank starts to reverse and so the discharge voltage increases slowly.

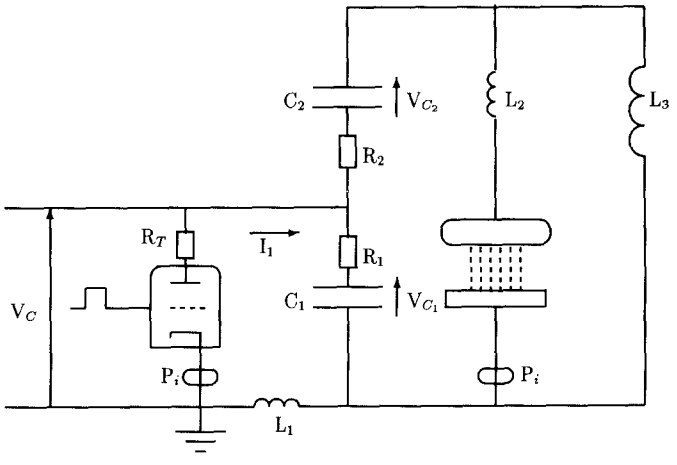

Fig. 2. L–C inversion electrical pumping circuit. Typical circuit parameters are the following: $C_1 = C_2 = 143$ nF; $L_1 = 175$ nH; $L_2 = 22$ nH; $L_3 = 28$ μH; $R_1 = R_2 = 0.01$ Ω; $R_T = 0.01$ Ω. P_i are for current probes

The following system of equations, included in the model, describes the temporal evolution of electric parameters of the equivalent circuit:

$$\frac{dI_d}{dt} = \left(L_3\frac{dI_3}{dt} - V_d\right)\frac{1}{L_2}, \quad (8)$$

$$\frac{dV_{C1}}{dt} = -(I_d + I_3 - I_1)\frac{1}{C_1}, \quad (9)$$

$$\frac{d^2I_3}{dt^2} = \left[(-I_d - I_3)\frac{1}{C_2} + \frac{dV_{C1}}{dt} - (R_1 + R_2)\left(\frac{dI_3}{dt} + \frac{dI_d}{dt}\right)\right]\frac{1}{L_3}, \quad (10)$$

$$\frac{dI_1}{dt} = (-(R_1 + R_T)I_1 - V_{C1})\frac{1}{L_1}, \quad (11)$$

where V_{C1} is the voltage of C_1 capacitor bank, I_d is the discharge current, I_1 is the thyratron current and I_3 is the current of the self-induction coil L_3, V_d is the discharge voltage across laser electrodes.

V_d is expressed as $V_d(t) = dE(t) = I_d(t)R_p(t)$, where R_p is the time-dependent plasma resistance and d the inter-electrode distance. $V_d(t)$ is then a secondary variable and is determined by the plasma state at time t. The third differential equation was transformed into two first order ones. So five differential equations must be solved.

The X-ray temporal and spectral distribution were calculated from experimental results of the X-ray generator: voltage and current of the cathode. X-ray absorption by materials separating the active medium from the X-ray generator was taken into account. The absorption of X-rays by xenon and neon resulted in a source term of free electrons and kinetic species [30].

1.5 Numerical Treatment

The method used for solving the time-dependant Boltzmann equation was already presented elsewhere [24, 25]. The eedf $n(\varepsilon, t)$ is discretized by a set of N variables representing $n(\varepsilon, t)$ in the energy intervals $[\varepsilon_i - w_i/2, \varepsilon_i + w_i/2]$ with increasing width w_i. The number K of energy bins is of the order of 100.

In the kinetic equations, all the terms connected to electron collisions are evaluated at each time step. The three sets of equations corresponding respectively to the eedf, the kinetic species and the electric circuit are grouped in a unique set of differential equations and then solved without decoupling of the three sets. Each process being labeled, as well as each category of the processes, the numerical code runs over the entire set of processes. For those involving electrons, their contribution to the time derivatives of the kinetic equations and of the electron distribution equations are calculated simultaneously. Internal tests verify that the particle density balances are identical for the eedf and kinetic equations.

Concerning the self-consistent integration of the system of differential equations, a key point is the coupling of the eedf set with electric equations. $n(\varepsilon_i, t)$ and I_d being considered as independent variables, at each time step, E/N is evaluated from (7) in which J_E is expressed in terms of the $n(\varepsilon_i, t)$ with help of relation (5) by using the finite difference method:

$$J_E = \sum_{i=1}^{K-1} (\varepsilon_{i+1} - \varepsilon_i)[J^+(b_i) - J^-(b_i)], \tag{12}$$

in which $J^+(b_i)$ and $J^-(b_i)$ correspond respectively to the classical writing of the upstream and downstream fluxes of electrons in the energy space due to the electric field heating evaluated at $b_i = \varepsilon_i + w_i/2$. This last equation results from the discretization of relation (5) with $J^+(b_i)$ and $J^-(b_i)$ respectively expressed as:

$$J^+(b_i) = A_i n(\varepsilon_i, t), \tag{13}$$

$$J^-(b_i) = B_i n(\varepsilon_{i+1}, t), \tag{14}$$

in which

$$A_i = \frac{2}{3}\frac{e^2}{m_e} N \frac{1}{\nu_{en}(b_i)} \left(\frac{b_i}{\varepsilon_{i+1} - \varepsilon_i} + \frac{1}{2}\mu_{1,i} \right), \tag{15}$$

$$B_i = \frac{2}{3}\frac{e^2}{m_e} N \frac{1}{\nu_{en}(b_i)} \left(\frac{b_i}{\varepsilon_{i+1} - \varepsilon_i} - \frac{1}{2}\mu_{2,i+1} \right), \tag{16}$$

and $\mu_{1,i} = (\varepsilon_{i+1} - b_i)/(\varepsilon_{i+1} - \varepsilon_i)$, and $\mu_{2,i+1} = (b_i - \varepsilon_i)/(\varepsilon_{i+1} - \varepsilon_i)$. In the expressions of A_i and B_i we neglect the influence of excited states on $\nu_{en}(b_i)$, and A_i and B_i are considered as being constant. From (12–16) we see that J_E can be linearized on the basis of the $n(\varepsilon_i, t)$ with constant coefficients which are calculated at the beginning of the code run. Therefore, we get a fast evaluation of E/N versus I_d and the $n(\varepsilon_i, t)$. Then E/N is inserted in the Boltzmann equation (1) and $V_d = E(t)d$ in (8) for the discharge current. Note that this procedure can be used for any electrical circuit. For another device, we have just to change the corresponding electric equations.

For the integration we used the LSODA solver which is well-suited for the resolution of stiff equations [31]. Its interest lies, in our case, in the fact that we deal with differential equations having very different characteristic evolution frequencies, the eedf evolving faster than species densities. It starts with the Adams-Moulton Predictor-Corrector method and automatically switches to the Gear ones. This second method was proved to be very efficient in terms of CPU time when we provided an explicit Jacobian of the system of equations. The Jacobian is more easily expressed by keeping the explicit dependences on the independant variables particularly for the crossed terms, for instance for the partial derivatives of $dn(\varepsilon_i, t)/dt$ with respect to the species density N_j, or for the partial derivatives of dN_j/dt with respect to the $n(\varepsilon_i, t)$. Due to the semi-automatic writing of the Boltzmann and kinetic equations, the generation of the Jacobian is done at the same time as the calculation of the differential equations. Let us mention, that the introduction of e–e Coulomb collisions needs some caution due to the quadratic dependences of the corresponding terms in the Boltzmann equation.

The resulting numerical code was implemented on a 486-33 MHz microcomputer, a typical run needs a CPU time of about one hour in order to describe the discharge until a few inversions of the discharge current.

2 Results

The main results which are given here correspond to the following standard conditions: Discharge volume is about 0.8 l (4.5 × 4 × 40 cm^3), charging voltage of 20 kV, total capacitance 286 nF and interelectrode distance of 4.5 cm in mixture containing 30 mbar of Xe, 3 mbar of HCl and 4000 mbar of Ne.

2.1 Discharge and Plasma Parameters

Figure 3 presents the temporal behaviour of the electrical parameters and of the laser power. Discharge breakdown appears before the total voltage inversion of C_1 capacitor bank, the maximum value of the discharge voltage reaches 30 kV, the corresponding value of the reduced electric field is about 7 Td. Then there is a fast increase of the discharge current followed by the starting of the laser power. A plateau in the discharge voltage is then established until the inversion of the discharge current.

Typical evolutions of species densities included in the kinetic reactions are given in Figs. 4, 5. The temporal evolution of ions is represented in Fig. 4. During the discharge, the density of Xe^+ ions which is the dominant ionic species leads the electron number density which reaches 10^{15} cm^{-3}. Let us mention that, in contrast Longo et al. [8], the $NeXe^+$ ion density is much lower than Xe^+ one; the difference probably lies, in addition to different electric circuits, in the three-body rate constants for the respective

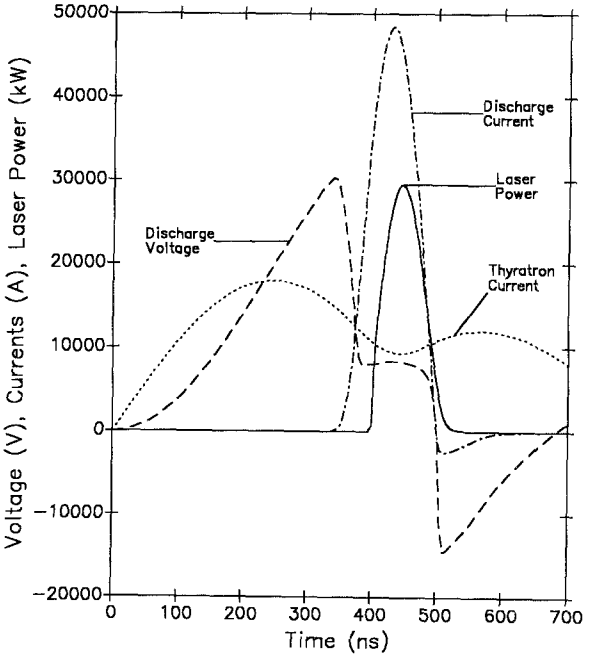

Fig. 3. Typical evolution of electrical parameters and laser power for a capacitor charging voltage $V_C = 20$ kV. The total presure is $P = 4$ bars with xenon and HCl partial pressures of respectively 30 and 3 mbars

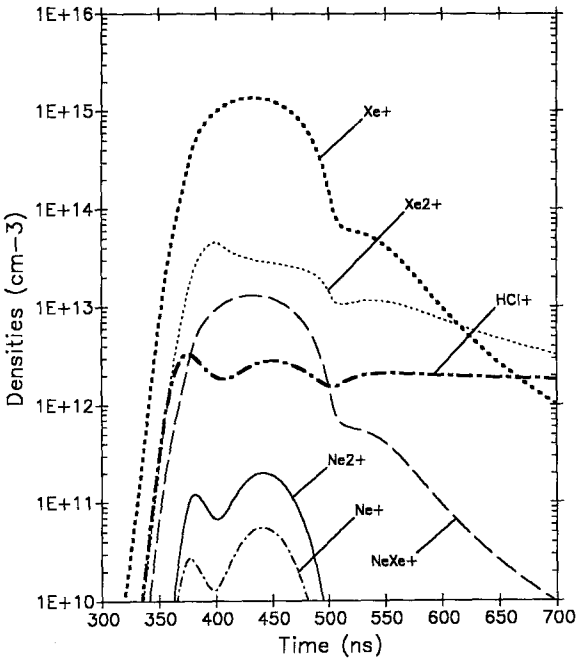

Fig. 4. Temporal evolution of main ion densities. Same conditions as for Fig. 3

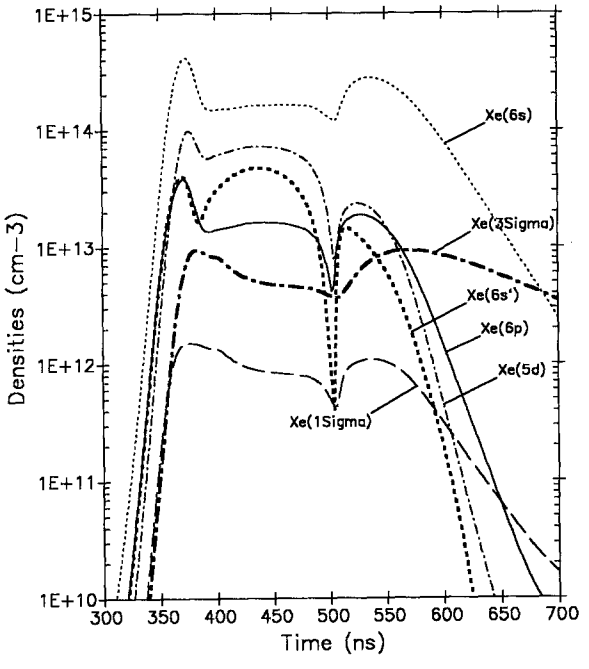

Fig. 5. Temporal evolution of some xenon excited state densities. Same conditions as for Fig. 3

formation of $NeXe^+$ and Xe_2^+ but other factors as the treatment of the stepwise ionization cannot be disregarded.

The populations of xenon excited states are given in Fig. 5. The main excited state of xenon is the Xe(6*s*). Meanwhile, the density of Xe(5*d*) is quite large and plays an important role in the ionization process as an intermediate state. During the voltage plateau, the ionization is dominantly yielded by the highest xenon excited states.

The population densities of neon excited and ionic

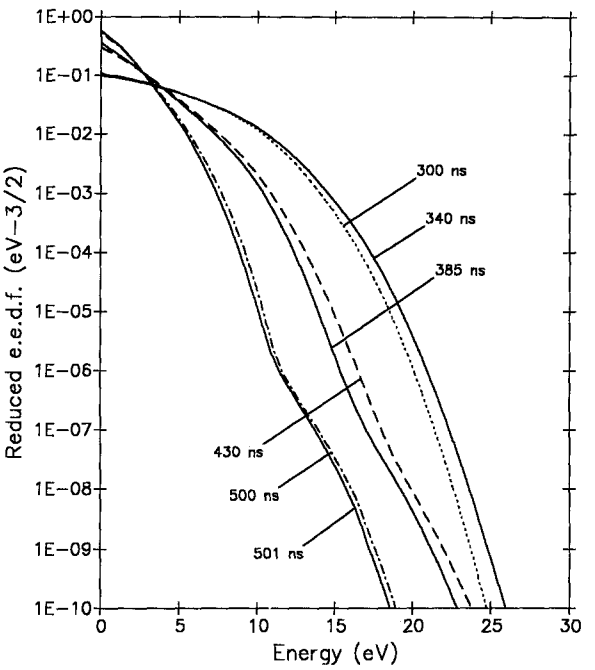

Fig. 6. Reduced eedf at different time in the discharge. Same conditions as for Fig. 3. The curves are labeled by figures corresponding to times indicated in the insert (see text)

states remains low (two orders of magnitude lower than the first excited level of xenon). So, it is not necessary to include more than one excited level of neon to model excimer lasers excited by transverse-electric discharges. The main role of neon is then to define the eedf through elastic electron–atom collisions, in addition to the role played in two- and three-body collisions between heavy species.

The evolution of the reduced electron energy distribution function $n(\varepsilon, t)/n_e\sqrt{\varepsilon}$ is represented in Fig. 6 at different times of the discharge development corresponding to Fig. 3. These times have been chosen in order to show the eedf first, during the electron heating by electric field as the voltage increases, second, during the discharge plateau (the time of 410 ns corresponds to a local minimum of the discharge voltage, and the time 430 ns to a local maximum) and, finally, during the discharge voltage inversion. As the discharge voltage and the excited species density increase, the effect of superelastic collisions begins to appear yielding shoulders in the eedf between 10 and 15 eV. These shoulders are due to superelastic collisions involving the main excited states, i.e., the xenon ones.

Note also that the absolute value of the reduced electric field is slightly higher for the time 501 ns ($E/N = -0.12$ Td) than for the dashed curve corresponding to 500 ns ($E/N = 0.10$ Td). These results illustrate that, for fast changes of E/N, the eedf cannot be strictly considered as being in stationary equilibrium with E/N. We discuss again this point later.

The influence of the internal energy stored on excited states is illustrated in Fig. 7 which gives, during the discharge history, the dependence of the drift velocity W_d and of the mean electron energy U_m versus E/N. The sense of increasing times is indicated by arrows. The two pathways

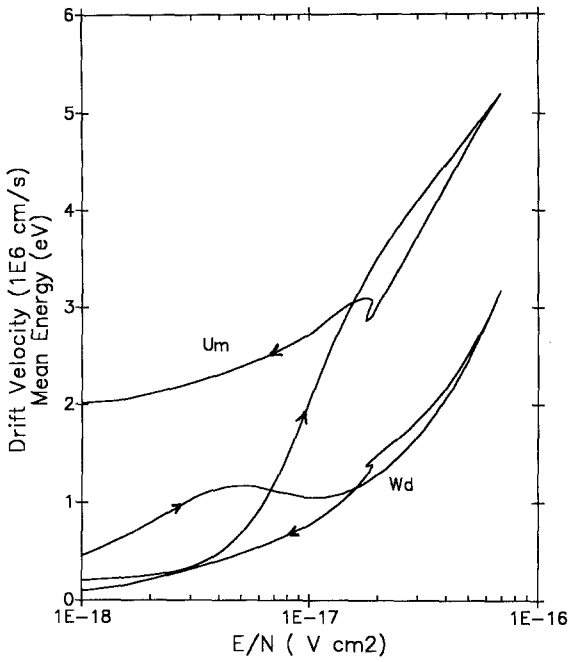

Fig. 7. Dependence of the drift velocity W_d and mean electron energy U_m vs E/N during the discharge development. Same conditions as for Fig. 3

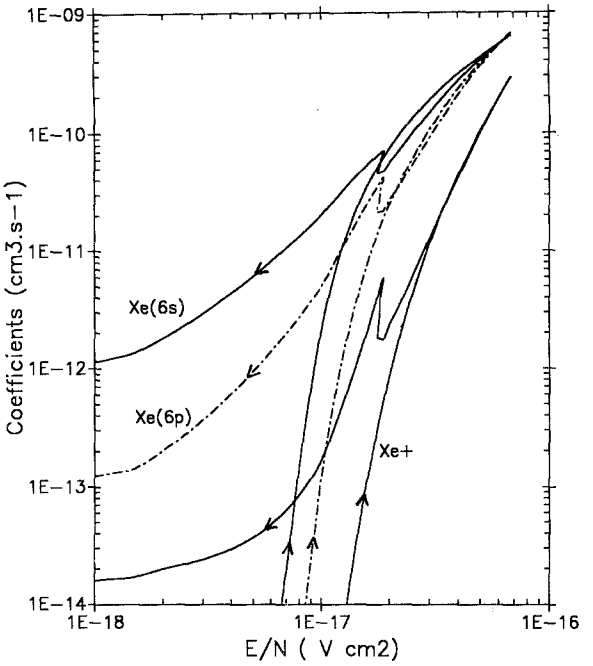

Fig. 8. Dependence of xenon ionization and excitation rates versus E/N during the discharge development. Same conditions as for Fig. 3

forth and back can be explained by the evolution of densities of excited states. Starting from low E/N values, the electron and excited state densities increase, the discharge establishes in a weakly excited and ionized gas. For electron density n_e and discharge current I_d becoming high, excited state densities achieve also high values (see Fig. 5), and the electron collision processes involving these excited states influence the transport parameters. Inelastic collisions and ionization processes tend to reduce the energy of electrons; during a first stage ($E/N > 2$ Td) the effect of superelastic collisions and Penning ionizations is insufficient to compensate this cooling of electrons. When the reduced electric field becomes lower ($E/N < 2$ Td), the reverse is observed: the heating effect of superelastic collisions and Penning ionization dominates. This produces a stabilization of U_m to rather high values ($U_m > 2$ eV).

The effect of high excited state densities is also observed for reaction rates corresponding to excitation and ionization by electron impact as shown in Fig. 8 which represents the dependence, versus E/N, of rates for direct ionization of Xe and excitation towards Xe(6*s*) and Xe(6*p*) states. During the voltage plateau, the rates corresponding to the formation of Xe(6*p*) and Xe^+ states are much greater than those obtained for the same voltage values during the early stage of the discharge development while that one corresponding to Xe(6*s*) is nearly unchanged. These effects still result from the competition between inelastic collisions on excited states and superelastic collisions.

Concerning these effects of excited states on the eedf, on plasma parameters and on transport coefficients, we must emphasize that they have to be included carefully in the laser model. If we consider the total electric energy delivered to the laser medium untill the voltage inversion, the fraction of the energy deposited before the establishing of the voltage plateau represents no more than 10%. During the initial stage of the avalanche development the discharge medium can be considered as weakly ionized. But in a second stage, when the discharge current increases and the voltage drops, new conditions for the discharge medium are achieved. In this situation, it is necessary to take account of the detailed repartition of the energy which is stored in the various excited and ionic states.

In connection with Figs. 7, 8, the particular behaviour of parameters reported in these figures near $E/N = 2$ Td at the end of the E/N fall following the breakdown needs to be discussed. The large changes of these parameters at quasi constant E/N can result from various effects: the increasing influence of e–e collisions as the electron density rises, the influence of superelastic collisions on the eedf and the non-stationarity of the eedf just at the end of the voltage fall. It is in fact difficult to discriminate the respective influence of these effects due to their coupling. However, from Fig. 5 we observe that during the voltage plateau the densities of main excited states are nearly constant, so, the effect of superelastic collisions cannot explain in itself this behaviour. Calculations done without e–e Coulomb collisions showed that in this case this behaviour is still amplified. Therefore, we can conclude that there is certainly an important effect of non-stationarity. The present results confirm the conclusions drawn by Winkler and Wuttke [16] that the possibility of observing non-stationarity between the eedf and E/N is more important at relatively low E/N values.

2.2 HCl *Kinetics and Excimer Formation*

Let us now present the results obtained for the influence of the vibrational distribution of HCl. The temporal evolu-

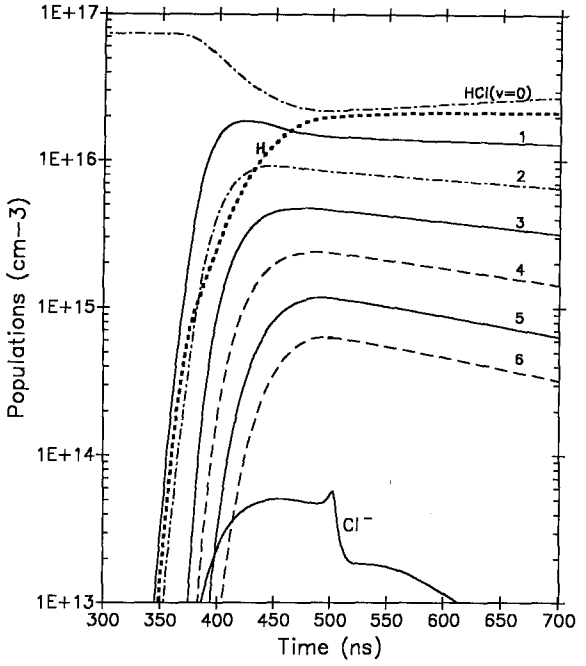

Fig. 9. Temporal evolution of HCl(v) vibrational populations and H and Cl^- densities. Same conditions as for Fig. 3

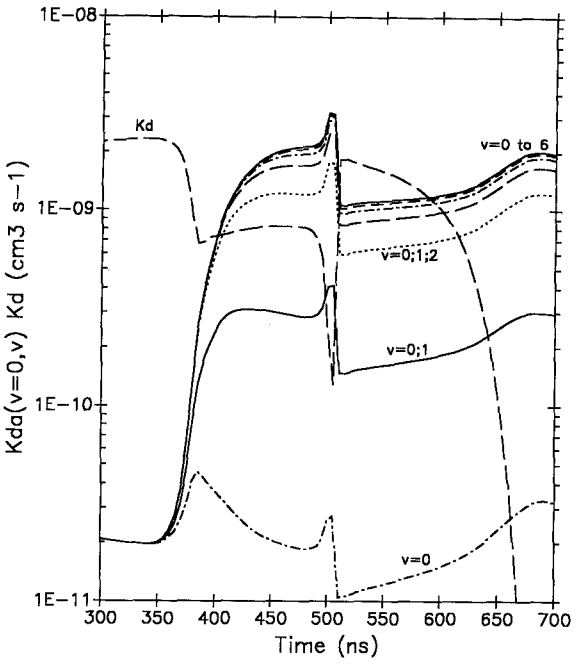

Fig. 10. Temporal evolution of contributions of excited vibrational states HCl(v) to dissociative attachment and of direct dissociation. Same conditions as for Fig. 3. For the different curves see text

tion of the vibrational populations N_v of HCl(v) and the H and Cl^- densities is reported in Fig. 9. Up to the formation of the discharge voltage plateau, populations of vibrationally excited states remain low. They increase fastly before the voltage plateau and then decrease slowly in the relaxation phase. In this last phase, the vibrational deactivation is mainly due to V–T processes by collision with H atoms which achieve densities of about 30% of the initial HCl density. Then, we can conclude that V–T and V–V processes mainly act during the post-discharge and their effect is probably of minor importance during the active phase of the discharge. These results are in qualitative agreement with those obtained by Longo et al. [17].

The influence of vibrational excitation on dissociative attachment coefficients is illustrated in Fig. 10, as a function of time. We have represented in this figure the contribution of the ground level and the partial sums of dissociative attachment coefficients for $v = 0, 1; v = 0, 1, 2, \ldots$, and, finally, the sum over the seven vibrational levels included in the model. We observe, as a function of time, a fast increase of the dissociative attachment total frequency and of contributions of vibrationally excited levels during the voltage plateau. This increase of the dissociative attachment rate must be attributed partly to the change of the eedf during this phase (electron mean energy is decreased) and mainly to the fast increase of the populations of vibrationally excited states. It is connected to the fast increase of the dissociative attachment cross-section from $v = 0$ to $v = 1$ and from $v = 1$ to $v = 2$. The total dissociative attachment coefficient is by two orders of magnitude higher than the contribution of the $v = 0$ vibrational level.

Regarding the problem of the number of HCl(v) vibrational states that we have to include in the model, we observe that the contribution to the dissociative attachment frequency of levels $v = 0$ to $v = 4$ is nearly the same as the total frequency. So, for a good approximation of the total dissociative attachment, at least four HCl excited vibrational levels have to considered in models.

We have also reported in Fig. 10 the evolution of the direct dissociation coefficient K_d. Up to the voltage plateau K_d is by about two orders of magnitude greater than the effective dissociative attachment coefficient K_{da}. During the voltage plateau it becomes lower than K_{da} but remains non negligible except for the late phase of the discharge.

In Fig. 11 we give the relative contributions of neutral and ionic channels to the formation of excimer molecule XeCl*. For the neutral channel, we have distinguished the channel involving HCl($v = 0$):

$$\mathrm{HCl}(v = 0) + \mathrm{Xe}^{**} \rightarrow \mathrm{XeCl}^* + \mathrm{H}\,,$$

where Xe** stands for xenon excited states higher than Xe(6s), from the channel involving vibrationally excited states:

$$\mathrm{HCl}(v > 0) + \mathrm{Xe}^* \rightarrow \mathrm{XeCl}^* + \mathrm{H}\,,$$

where Xe* corresponds to any excited xenon state. The ionic channel is dominant during the laser pulse but the total contribution of the neutral channel cannot be neglected.

The repartition of the power density dissipated by electrons in various processes is given in Fig. 12 as a function of the reduced electric field E/N. Here again, this figure represents the history of the discharge in the sense that the results are influenced by the excited state densities. We first observe that, due to the effect of superelastic collisions the net energy involved in inelastic and superelastic collisions is lower during the voltage plateau. Second, the energy

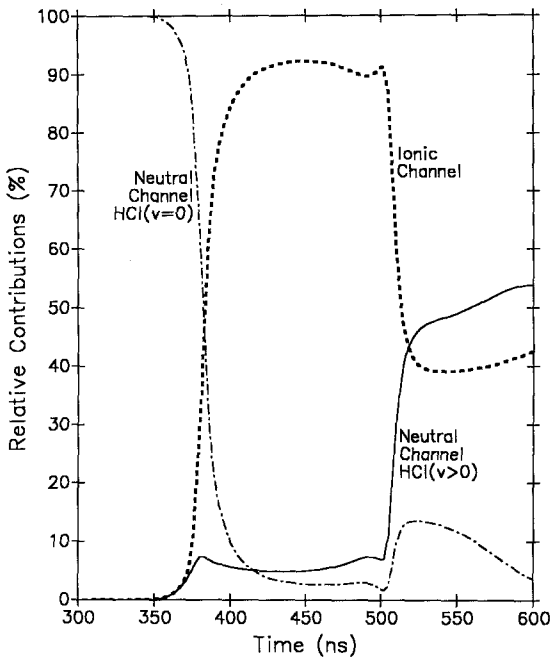

Fig. 11. Relative contributions (in %) of neutral and ionic channels to the formation of XeCl*. Same conditions as for Fig. 3

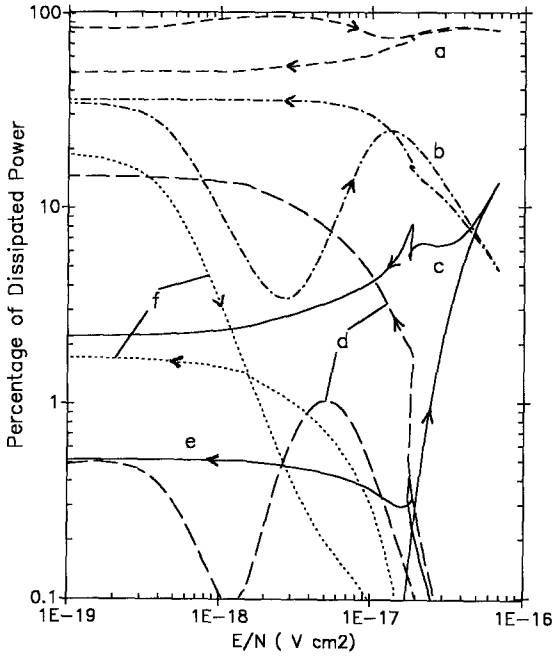

Fig. 12. Power density dissipated by electrons in various processes as a function of E/N during the discharge. The sense of time is indicated by arrows. a: net energy for inelastic and superelastic collisions, b: elastic electron-atom and electron-molecule collisions, c: ionization, d: dissociative attachment, e: dissociative recombination, f: Penning ionization (energy delivered to electrons). Same conditions as for Fig. 3

dissipated in dissociative attachment is non-negligible particularly during this plateau when HCl(v) excited vibrational states are highly populated. Third, in the high electron density phase, the energy involved in ionization processes is important and very different from that corresponding to the avalanche development phase. This is the the result of both effects of the modification of the eedf by superelastic collisions (see Fig. 6) and of the ionization of excited states. Finally, we observe that the energy yielded to electrons by Penning processes remains small except during the early stage of the avalanche development and during the voltage inversion when the electric field heating is low.

2.3 *Influence of Electron–Electron Coulomb Collisions*

Due to the limitation of the electron density by dissociative attachment of electrons on HCl, the influence of e–e Coulomb collisions on the results of the modelling is generally thought as being of minor importance. We must recall that the electron density achieves values of the order of 10^{15} cm^{-3} and, so, for typical pressures of a few atmospheres, the ionization degree achieves values of the order of 10^{-5}, which is sufficient to observe some effect.

This effect on the eedf is illustrated in Fig. 13 which gives the reduced eedf for E/N values which correspond to the voltage plateau ($E/N \leq 2$ Td). Large differences between solid lines (electron–electron Coulomb collision included) and dotted or dashed lines (e–e collisions excluded) is observed. In the energy range 12–20 eV, the eedf is by far less populated when we do not consider e–e collisions. As a consequence, the collision rates corresponding to inelastic collisions having energy thresholds higher than about 10 eV are significantly reduced. This is particularly the case for direct ionization of xenon atoms; in effect, without e–e collisions, we observed a reduction of the corresponding rate by an order of magnitude or more during the voltage plateau with respect to values obtained with e–e collisions.

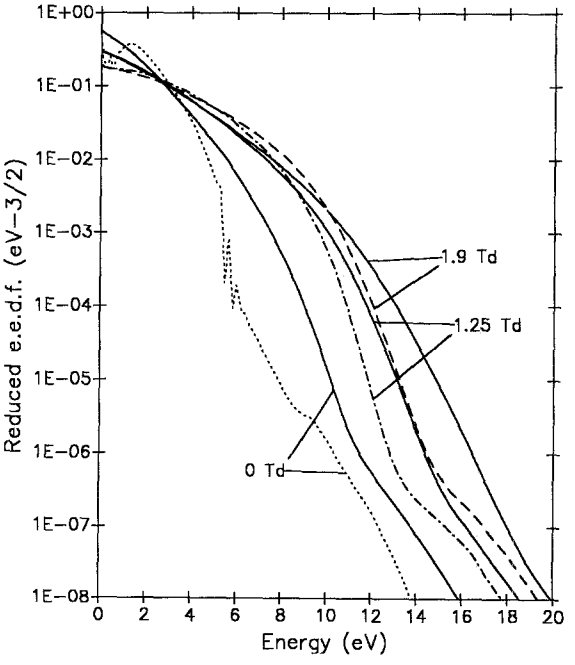

Fig. 13. Influence of e–e Coulomb collisions on the eedf during the discharge plateau and the voltage inversion. Same conditions as for Fig. 3. Dotted and dashed lines: without e–e collisions; full lines: with e–e collisions

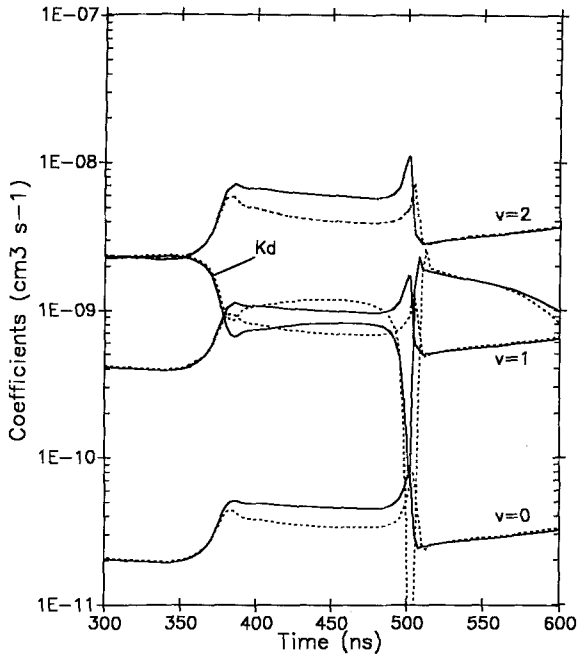

Fig. 14. Influence of e–e Coulomb collisions on dissociative attachment coefficients for vibrational states $v = 0$ to 2 and on the average direct dissociation coefficient. Full curves: with e–e collisions; dotted curves: without e–e collisions. Same conditions as for Fig. 3

Results for Xe* excited states depend of the levels that we consider: for Xe(6s) states the excitation rate is nearly unchanged while, for Xe(6p) ones, it is noticeably reduced.

We also observe large differences in the low-energy range of the eedf, for relatively low E/N values. This is a well known result: e–e collisions are also important in the low-energy range, they smooth the structures in the eedf which appear in connection with peaks in the inelastic cross-sections. As a consequence, dissociative attachment coefficients suffer important modifications. This effect is illustrated in Fig. 14 which gives the temporal evolution of dissociative attachment coefficients on HCl(v) for $v = 0$ to $v = 2$ and the dissociative attachment coefficient K_d averaged over the vibrational distribution. We observe, during the voltage plateau, that when we consider e–e collisions these coefficients are increased by a factor of about 1.5 with respect to values obtained without e–e collisions. On the contrary, the direct dissociation coefficient is decreased by about the same factor. At the same time, the HCl(v) vibrational distribution is nearly unchanged, the net result is that the Cl^- density is also increased by a factor of about 1.5.

We have found a small increase of the electron density when we do not consider e–e collisions: the maximum electron density for our standard experimental conditions was found to be 1.55×10^{15} cm^{-3} without Coulomb collisions, while it was 1.37×10^{15} cm^{-3} when e–e collisions are considered. If we keep in mind that the dominant ion species is Xe^+ and that the main channel for XeCl* formation is the Cl^-–Xe^+ recombination, the final result is that the XeCl* density and therefore the predicted laser power and energy are slighly reduced, by about 20%, when we neglect Coulomb collisions in the model.

Thus, including or not e–e collisions changes appreciatly the results of the model. These results are similar to those given by Longo et al. [8] despite the fact that these authors considered only the vibrational levels $v = 0$ and $v = 1$.

3 Comparison with Experimental Results and Discussion

The validation of any laser model would require, in addition to common diagnostics of the electrical parameters and of the laser power and energy, a number of experimental diagnostics in order to check the importance of key species of the kinetic model. In particular, it appears that diagnostics of Xe* excited state densities [11, 32] are very useful as well as those which could be undertaken on HCl(v) populations and derived species [33].

In the case of the present experimental device, we had only the possibility to compare electrical parameters and laser output. Thyratron and discharge currents obtained in the experiment and predicted by the model are compared in Fig. 15 for a capacitor charging voltage of 20 kV, a total pressure of 4 bars with 30 mbars of xenon and 3 mbars of HCl. Current waveforms are well predicted by the model but the value of the discharge current is too high.

Disregarding problems connected with experimental measurements of high pulsed discharge currents, we have tried to test the influence of both ionization processes and dissociative attachment on the discharge current given by the model. Except for the case in which we completely neglected the ionization of excited states, when we changed the number of xenon excited levels considered for stepwise excitation, we did not find significant modifications of the results for the discharge current peak. The influence of

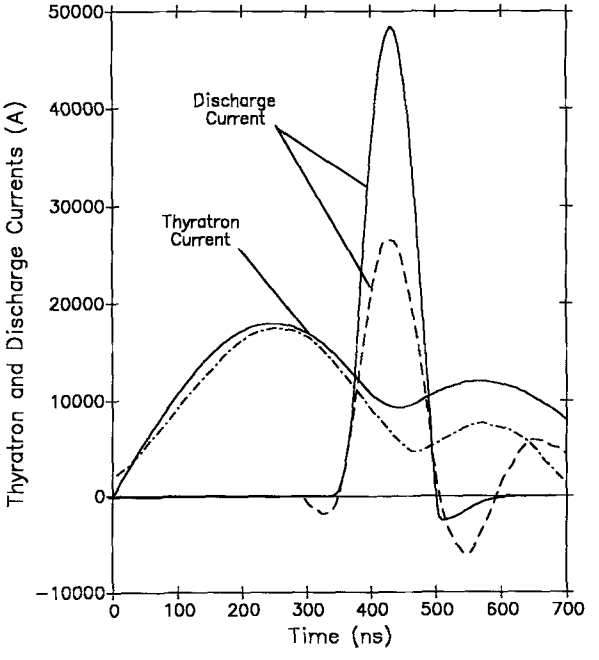

Fig. 15. Comparison between experimental and theoretical discharge and thyratron current waveforms. Same conditions as for Fig. 3. Full lines: model; dashed lines: experiment

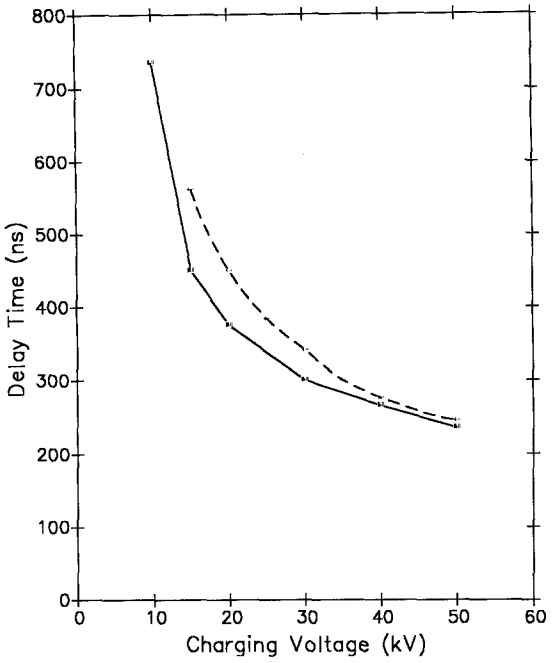

Fig. 16. Delay between thyratron switch and the breakdown. Same laser mixture as for Fig. 3. Dotted lines: experiment; full lines: model

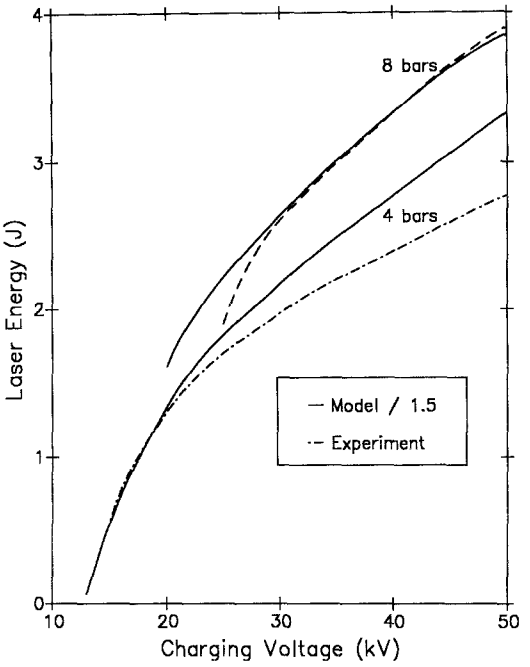

Fig. 17. Laser energy versus charging voltage (4 and 8 bars). The xenon and HCl partial pressures were kept constant to respectively 30 and 3 mbars. Dotted lines: experiment; full lines: results of the model divided by 1.5

dissociative attachment was tested by suppressing the contribution of the highest HCl(v) vibrational states. The effect on the maximum of the discharge current was still limited but we observed that the negative alternance of the current and later oscillations were better predicted by the model. In effect, with the seven vibrational levels included, the discharge current predicted by the model vanishes quite completely after the voltage inversion while in the experiment it continues to oscillate during a few periods.

A method to test the validity of the model for the avalanche development phase is to compare the delay time beetween the preionization and the formation of the discharge plateau [34]. This permits to check, for various discharge conditions and gas mixture compositions, the discharge transport coefficients (electron drift velocity, electron mobility, ionization ratee, etc.). We give in Fig. 16, for our experimental device, a comparison between experimental and theoretical results for the dependence of this delay time upon the charging voltage. We observe a relatively good agreement between these results. Nevertheless, delay times obtained from the model are slightly lower. This result is similar to that one obtained by Bötticher et al. [33]. We cannot exclude the explanation given by these authors based on the existence of the voltage cathode fall [35] which is not accounted for in 0-D positive column discharge models and which, in fact, reduces the E/N effective values. In the present experiment, the gas mixture contains also helium which is used as a buffer gas for HCl. We tested a possible influence of helium on the transport coefficients by introducing it as a fourth gas and considering elastic electron-helium atom collisions, we found a very low effect.

We did extensive comparisons for the laser energy obtained in the experiment and yielded by the model. We report in Fig. 17 the dependences of the laser energy versus the charging voltage for two values of the total pressure. We must mention that for this comparison, when we obtained from the model multiple laser pulses, we only took into account the first one; this situation was particularly encountered for high charging voltages. We notice that the trends for experimental and theoretical results are very similar but predicted values are by a factor of about 1.5 higher. Comparisons done for the influence of other parameters such as total capacitance values, interelectrode distance, etc., also led to a good agreement for the variations of the laser energy despite the systematic factor of 1.5 between experiment and model.

It is well known that many possibilities exist to fit theoretical results with those of a particular experiment by adjusting critical data of a model. Among these data we can mention the stimulated emission cross-section σ_{st}, the quenching coefficients of XeCl* by electrons and heavy particles, the existence of the slightly bouned XeCl(X) excimer ground state, and the choice of the quenching rates for this state, etc. We systematically studied the influence of some of these data on the results of the model. For the influence of σ_{st}, we indeed get some effect but its influence on the laser output energy was too low to explain the factor of 1.5 that we found without being out of the range of admitted values for σ_{st}, i.e., between about 2 and 5 $\times$ 10^{-16} cm^2. The same negative result was obtained for the quenching of XeCl* which was already discussed by Johnson et al. [3]. The most sensitive parameter was found to be the dissociation rate of XeCl(X) by heavy particles: as the dissociation rate of XeCl(X) was decreased, the laser energy output was also significantly decreased and a possible fit of experimental and theoretical results was possible. But due to the uncertainties on the previously mentioned parameters the choice for this last parameter is not un-

ambigous. For the main results given here we used for σ_{st} a value of 4×10^{-16} cm^2 and a dissociation rate of XeCl(X) by neon atoms (dominant quenching species) of 4×10^{-12} cm^3 s^{-1}.

Another point which merits some attention is that one of the existence and the influence of high-lying vibrationnally HCl(v) excited states. We have previously mentioned the effect of the limitation of the vibrational excitation on the discharge current particularly after the discharge voltage and current inversions. This problem of the vibrational excitation has been already discussed in the literature. Johnson et al. [3] reduced the vibrational excitation coefficients by a factor of about 10 in order to fit theoretical results with experimental ones obtained by Center et al. [36] for the vibrational distribution in an electron-beam-pumped XeCl laser. This limitation of the vibrational excitation was also proved by Longo et al. [8] to be very efficient to reduce the XeCl*density in discharge-sustained laser. However, this limitation seems arbitrary and does not agree with experimental data for vibrational excitation cross-sections [37, 38]. The behaviour of the discharge current after the voltage inversion as well as the reduction of the Cl^- density and, as a consequence, a decrease of the laser energy could be explained by the HCl depletion. In fact, as mentioned previously, the dissociation of HCl is not negligible for our conditions. We already mentioned an HCl dissociation of about 30%, but much higher values were found, particularly for low partial HCl pressures.

We give in Fig. 18 a comparison of the laser energy predicted by the model and obtained in the experiment as a function of the HCl partial pressure. The total pressure was kept constant to 5.65 bars as well as a ratio of 5 for the xenon partial pressure to the HCl one. The results of the model have still be divided by a factor of 1.5. We observe similar trends for the two curves but the experimental one presents a maximum for a lower value of the HCl pressure and decreases more rapidly. For an HCl partial pressure of 2 mbars, the HCl dissociation degree achieves a value of 50% at the end of the laser pulse. It decreases as the HCl pressure increases, it is of 26% for $P_{HCl} = 15$ mbars. The analysis of the results of the model indicates that the HCl depletion plays some role for the lowest HCl partial pressures but this role is probably minor for the highest ones. Let us recall that the main channel for the HCl depletion is the dissociative attachment and so, results depend strongly, from one model to another, on the manner in which the vibrational excitation and the dissociative attachment are treated. We must add that, for the highest HCl partial pressure that we consider here, the laser discharge was found experimentally as very unstable and the laser energy varied in a large range from one shot to another. These instabilities which are well-known for high HCl partial pressures [39, 40] could explain the differences observed for the two curves of Fig. 18. Indeed, they cannot be accounted for in our model, their study needs the use of 1-D or 2-D numerical models.

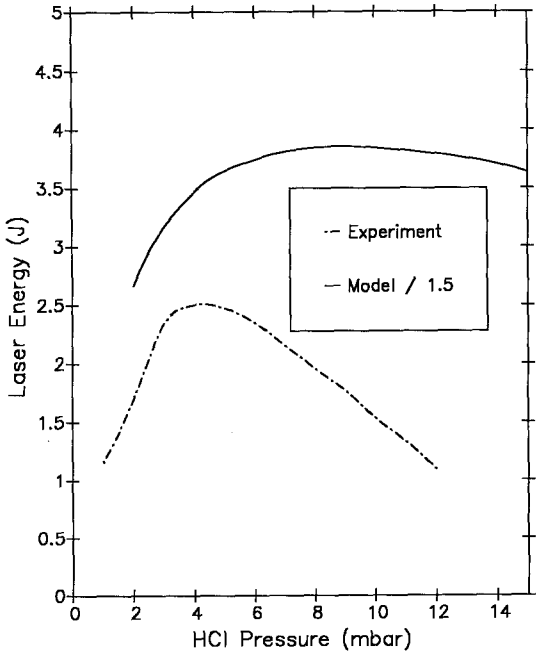

Fig. 18. Influence of the HCl partial pressure on the laser energy. The total pressure was $P = 5.65$ bars, the xenon partial pressure was fixed to 5 times the HCl pressure and the capacitor charging voltage to $V_C = 35$ kV. Dotted lines: experiment; full lines: model

4 Conclusion

The model that we present here for XeCl laser discharge permits to treat self-consistently the coupling between the non-equilibrium and non-stationary aspects of the eedf and kinetic species densities. We have emphasized the role of excited states on the modification of the transport and plasma parameters (electron drift velocity and mean energy, excitation and ionization coefficients). This role is particularly important for the discharge voltage plateau during which the major part of the electrical energy is transferred to the laser medium. We have shown that, despite the attaching effect of HCl, e–e Coulomb collisions modify significantly the discharge parameters, the electron collision rates and the extracted laser energy.

Concerning the HCl(v) vibrational kinetics and its consequences on the dissociative attachment, our results indicate that with actual data about HCl we must take account of vibrational levels till, at least, $v = 4$. With the data that we used, we have found that the HCl depletion is not negligible, particularly for low HCl partial pressures.

The results of the model have been compared with some experimental results for a X-ray preionized laser discharge working with a L–C inversion electrical pumping circuit. Despite a factor of about 1.5 between the laser energies given by the model and obtained in the experiment, we found similar trends for their variations versus various discharge conditions. This systematic factor can be modified by adjusting some key rate constants, but this choice does not appear as unique. Further experimental and theoretical investigations are still necessary to determine more precisely these constants and, also, to get a better understanding of the HCl kinetics.

Acknowledgements. This work is part of the Eureka Program E.U. 205 and of the C.N.R.S. French research group G.d.R.

Lasers à Excimères. The authors greatly acknowledge M. Legentil, R. Riva and V. Puech for many fruitful discussions and G. Comunale for her participation to this work. They are grateful to M. Capitelli, C. Gorse and S. Longo for the permission to use their set of data relative to HCl kinetics.

References

1. J. Levin, S. Moody, E. Klosterman, R. Center, J. Ewing: IEEE J. **QE-17**, 2282 (1981)
2. F. Kannari, A. Suda, M. Obara, T. Fujioka: IEEE J. **QE-19**, 1587 (1983)
3. T. Johnson, H. Cartland, T. Genoni, A. Hunter: J. Appl. Phys. **66**, 5707 (1989)
4. F. Kannari, W.D. Kimura, J.J. Ewing: J. Appl. Phys. **68**, 2615 (1990)
5. M. Maeda, A. Takahashi, T. Mizunami: Jpn. J. Appl. Phys. **21**, 1161 (1982)
6. H. Hokazono, K. Midorikawa, M. Obara, T. Fujioka: J. Appl. Phys. **56**, 680 (1984)
7. C. Gorse, M. Capitelli, A. Dipace: J. Appl. Phys. **67** (1990)
8. S. Longo, C. Gorse, M. Capitelli: IEEE Trans. PS—**19**, 379 (1991)
9. M. Turner, P. Smith: IEEE Trans. PS—**19**, 350 (1991)
10. A. Dem'yanov, V. Egorov, I. Kochetov, A. Napartovich, A. Pastor, N. Penkin, P. Serdobintsev, N. Shubin: Sov. J. Quant Electron., **16**, 817 (1986)
11. Th. Hammer, W. Bötticher: Appl. Phys. B **48**, 73 (1989)
12. C. Gorse: Non-Equilibrium Processes in Partially Ionized Gases, ed. by M. Capitelli, J.N. Bardsley (Plenum, New York, 1990) p. 411
13. C. Gorse, M. Capitelli, S. Longo, E. Estocq, J. Bretagne: J. Phys. D: Appl. Phys. **24**, 1947 (1991)
14. M. Capitelli, C. Gorse, S. Longo, J. Bretagne, E. Estocq: In Proc. SPIE Topical Meeting, Excimer Lasers and Applications. III, SPIE **1503**, 126 (1991)
15. M. Lando, Z. Rozenberg, M. Rokni: J. Appl. Phys. **68**, 2606 (1990)
16. R. Winkler, M.W. Wuttke: Appl. Phys. B **54**, 1 (1992)
17. S. Longo, M. Capitelli, C. Gorse, A. Dem'yanov, I. Kochetov, A. Napartovich: Appl. Phys. B **54**, 239 (1992)
18. B. Godard, E. Estocq, F. Joulain, P. Murer, M. Stehle, J. Bonnet, D. Pigache: SPIE Excimer Lasers and Applications III, **1503** (1991)
19. B. Godard, E. Estocq, P. Murer, M. Stehle, J. Bonnet. D. Pigache: Proc. 8th Int'l Symp. on Gaseous and Chemical Laser, Madrid (1990)
20. E. Estocq: Ph.D. Thesis, Université Paris-Sud, Orsay (1992)
21. M. Capitelli, M. Dilonardo, C. Gorse: Chem. Phys. **43**, 403 (1979)
22. D. Teillet-Billy, J.P. Gauyacq: J. Phys. B: At. Mol. Phys. **17**, 4041 (1984)
23. C. Gorse, M. Capitelli, M. Bacal, J. Bretagne: Chem. Phys. **102**, 1 (1986)
24. J. Bretagne, G. Delouya, J.L. Godart, V. Puech: J. Phys. D: Appl. Phys. **14**, 1225 (1981)
25. J. Bretagne, J.L. Godart, V. Puech: J. Phys. D: Appl. Phys. **15**, 2205 (1982)
26. J. Bretagne, M. Capitelli, C. Gorse, V. Puech: Europhys. Lett. **3**, 1179 (1987)
27. V. Puech, S. Mizzi: J. Phys. D: Appl. Phys. **24**, 1974 (1991)
28. W.L. Wiese, M.W. Smith, B.M. Glennon: Atomic Transition Probabilities, Nat. Bur. Stand. Ref. Data Series—NBS 4, Vol. I (Washington, DC 1966)
29. M. Aymar, M. Coulombe: Atom. Data Nucl. Data Tables **21**, 537 (1978)
30. J. Bretagne, Y. Louvet: J. Appl. Phys. **61**, 827 (1987)
31. R.C. Aiken: Stiff Computation (Oxford Univ. Press, Oxford 1985)
32. M. Legentil, S. Pasquiers, V. Puech, R. Riva: 11th Int'l Conf. on Spectral Lines Shapes, Carry-le-Rouet (France), June 8–12 1992
33. W. Bötticher, H. Lück, St. Niesner, A. Schwabedissen: Appl. Phys. B **54**, 295 (1992)
34. M. Legentil, S. Pasquiers, V. Puech, R. Riva: J. Appl. Phys. **72**, 879 (1992)
35. A. Belasry, J.P. Boeuf, L. Pitchford: Submitted to J. Appl. Phys.
36. R.E. Center, J.H. Jacob, M. Rokni, Z. Rozenberg: Appl. Phys. Lett. **41**, 116 (1982)
37. K. Rohr, F. Linder: J. Phys. B: Atom. Molec. Phys. **9**, 2521 (1976)
38. W.L. Morgan: JILA Data Center Report, No. 34 (June 1991)
39. J. Coutts, C.E. Webb: J. Appl. Phys. **59**, 704 (1986)
40. M.R. Osborne, M.H.R. Hutchinson: J. Appl. Phys. **59**, 711 (1986)